

ARTICLE

Open Access

Bulk CsPbCl_xBr_{3-x} (1 ≤ x ≤ 3) perovskite nanocrystals/polystyrene nanocomposites with controlled Rayleigh scattering for light guide plate

Chongming Liu¹, Zhicheng Zhu¹, Kaibo Pan¹, Yuan Fu¹, Kai Zhang¹ and Bai Yang¹✉

Abstract

Perovskite nanocrystals (PNCs)/polymer nanocomposites can combine the advantages of each other, but extremely few works can achieve the fabrication of PNCs/polymer nanocomposites by bulk polymerization. We originally adopt a two-type ligand strategy to fabricate bulk PNCs/polystyrene (PS) nanocomposites, including a new type of synthetic polymerizable ligand. The CsPbCl₃ PNCs/PS nanocomposites show extremely high transparency even the doping content up to 5 wt%. The high transparency can be ascribed to the Rayleigh scattering as the PNCs distribute uniformly without obvious aggregation. Based on this behavior, we first exploit the potential of PNCs to serve as scatters inside light guided plate (LGP), whose surface illuminance and uniformity can be improved, and this new kind of LGP is compatible with the advanced liquid crystal display technology. Thanks to the facile composition adjustment of CsPbCl_xBr_{3-x} (1 ≤ x ≤ 3) PNCs, the Rayleigh scattering behavior can also be adjusted so as to the performance of LGP. The best-performing 5.0-inch LGP based on CsPbCl_{2.5}Br_{0.5} PNCs/PS nanocomposites shows 20.5 times higher illuminance and 1.8 times higher uniformity in display than the control. The LGP based on PNCs/PS nanocomposite exhibits an enormous potential in commercialization no matter based on itself or combined with the LGP-related technology.

Introduction

In recent years, perovskite nanocrystals (PNCs) have become an attractive material due to their wonderful properties such as defect tolerance, facile synthesis, high photoluminescence with narrow bandwidth and easily tunable bandgap through size or composition adjustment^{1–3}. Despite the extraordinary properties of PNCs, they suffer from instability, especially when exposed to light, moisture, polar solvents, and high temperature, as their dynamic nature of the perovskite lattice and ligand binding^{2,4,5}. The instability discounts their performance and limits their further application.

The fact that nanoparticle and polymer hybrid materials can often combine the advantages of each has been demonstrated in several fields^{6–9}. Embedding PNCs into polymer is an effective strategy to enhance the PNCs

stability and polymer can endow the PNCs with other positive effects based on different structure and functional groups, such as surface defect passivation¹⁰, facilitating the charge separation and transport¹¹, assisted self-assembly and controlled morphology^{12–14}, and excellent processability, stretchability, and mechanical property in the form of nanocomposites¹⁵. Therefore, PNCs/polymer nanocomposite is promising for displays^{15–17}, luminescent solar concentrators^{18,19}, scintillator^{20,21}, lighting^{22–24} and hybrid photovoltaic device^{25,26}. The uniform distribution of PNCs in polymer matrix is critical to the properties of the nanocomposites and the aggregation of PNCs induced by high surface energy has a severe influence on the performance of related applications^{27–31}. As such, the loading fraction is limited owing to the phase separation between PNCs and polymer. Chemical interaction between PNCs and polymer is necessary to suppress the phase separation.

Correspondence: Bai Yang (byangchem@jlu.edu.cn)

¹State Key Laboratory of Supramolecular Structure and Materials, College of Chemistry, Jilin University, 130012 Changchun, China

© The Author(s) 2023



Open Access This article is licensed under a Creative Commons Attribution 4.0 International License, which permits use, sharing, adaptation, distribution and reproduction in any medium or format, as long as you give appropriate credit to the original author(s) and the source, provide a link to the Creative Commons license, and indicate if changes were made. The images or other third party material in this article are included in the article's Creative Commons license, unless indicated otherwise in a credit line to the material. If material is not included in the article's Creative Commons license and your intended use is not permitted by statutory regulation or exceeds the permitted use, you will need to obtain permission directly from the copyright holder. To view a copy of this license, visit <http://creativecommons.org/licenses/by/4.0/>.

Meanwhile, most of the fabrication methods of PNCs/polymer nanocomposites are spin coating, swelling-shrinking and electrospinning based on the in situ synthesis of PNCs in polymer matrix and physical mixing^{5,32}. To enhance the chemical anchoring of polymers onto PNCs, there are also quite a number of researches about the structural design of polymer with functional groups. The polymers always act as ligands or host matrices, including ammonium bromide or carboxyl-functionalized polystyren^{31,33}, zwitterion-containing copolymers^{10,27}, polyacrylic acid-grafted graphene oxide³⁴, polyvinyl pyrrolidone³⁵, carboxyl or amino-functionalized poly(ethylene glycols)¹², poly(maleic anhydride-alt-1-octadecene)³⁶, hydrolyzed poly(methyl methacrylate)/highly branched poly(ethylenimine)³⁷, etc.

However, extremely few works can satisfy the bulk polymerization to fabricate nanocomposites, where polymerizable capping agents play an important role to disperse PNCs into polymer matrix uniformly. In 2017, Sun et al. first synthesized 4-vinyl-benzyl-dimethyloctadecylammonium chloride as a polymerizable ligand, whose ammonium group can interact with MAPbBr₃ PNCs and the styryl group can help MAPbBr₃ PNCs copolymerize with styrene and methyl methacrylate to obtain homogeneous bulk MAPbBr₃ PNCs/polymer nanocomposites³⁸. Methacrylic acid modified PNCs copolymerized with hydrophobic methyl methacrylate and methacrylisobutyl polyhedral oligomeric silsesquioxane monomers were also reported and the nanocomposites show excellent luminescent performance and stability^{30,39}. Recently, Li et al. found zinc methacrylate can stabilize the CsPbBr₃ PNCs in polymethyl methacrylate matrix by replacing the surface ammonium ligands²⁸. Based on the strong ion-dipole interactions between the CF₃ of fluorinated acrylate and the positively charged PNCs, Liu et al. fabricated luminescent PNCs/fluorinated polymers nanocomposites, exhibiting stretchable and self-healable properties and high resistance to a harsh environment⁴⁰. Nevertheless, the loading fraction of PNCs in nanocomposites is typically at an extremely low level <1.0 wt% accompanied by slight aggregation, which means a further effective strategy is demanded for suppressing the phase separation.

Therefore, in this work, we adopted a two-type ligand strategy to fabricate PNCs/polystyrene (PS) nanocomposites, where the undec-10-en-1-amine (EAm) help PNCs disperse in styrene and the synthetic bis[(4-ethenylphenyl)methyl]dimethylammonium chloride (BEMDA) works as polymerizable capping ligands to endow the PNCs with polymerization activity. The bulk CsPbCl₃ PNCs/PS nanocomposites can still maintain high transparency even at the doping content up to 5 wt%. We ascribed the high transparency to the uniform distribution of PNCs in PS matrix, which means the scattering of light can be described by Rayleigh theory. Additionally, the high

refractive index of perovskite materials has been reported in recent years^{41–44}, while the potential effects and applications related to their high refractive have not drawn much attention as their photovoltaic and luminescent properties did^{42,45,46}. We focus on the Rayleigh scattering inside the nanocomposites caused by the higher refractive index of PNCs than PS. We found PNC can be a type of scatter inside PS-type light guide plate (LGP) enhancing the on-surface illuminance and uniformity. We also systematically studied the mechanism of the improved surface illuminance and the influence of different PNC compositions CsPbCl_xBr_{3-x} ($1 \leq x \leq 3$) on the performance of LGP. The refractive index of PNCs can be adjusted from 1.70 to 2.02 at 450 nm for CsPbCl_xBr_{3-x} ($1 \leq x \leq 3$) PNCs. For 5.0-inch LGP, the best performing LGP doping with 1 wt% CsPbCl_{2.5}Br_{0.5} PNCs exhibits about 20.5 times higher illuminance and 1.8 times higher uniformity in display than the control. This new kind of LGP based on the PNCs/PS nanocomposite is compatible with advanced liquid crystal display (LCD) technology, indicating great value in practical application.

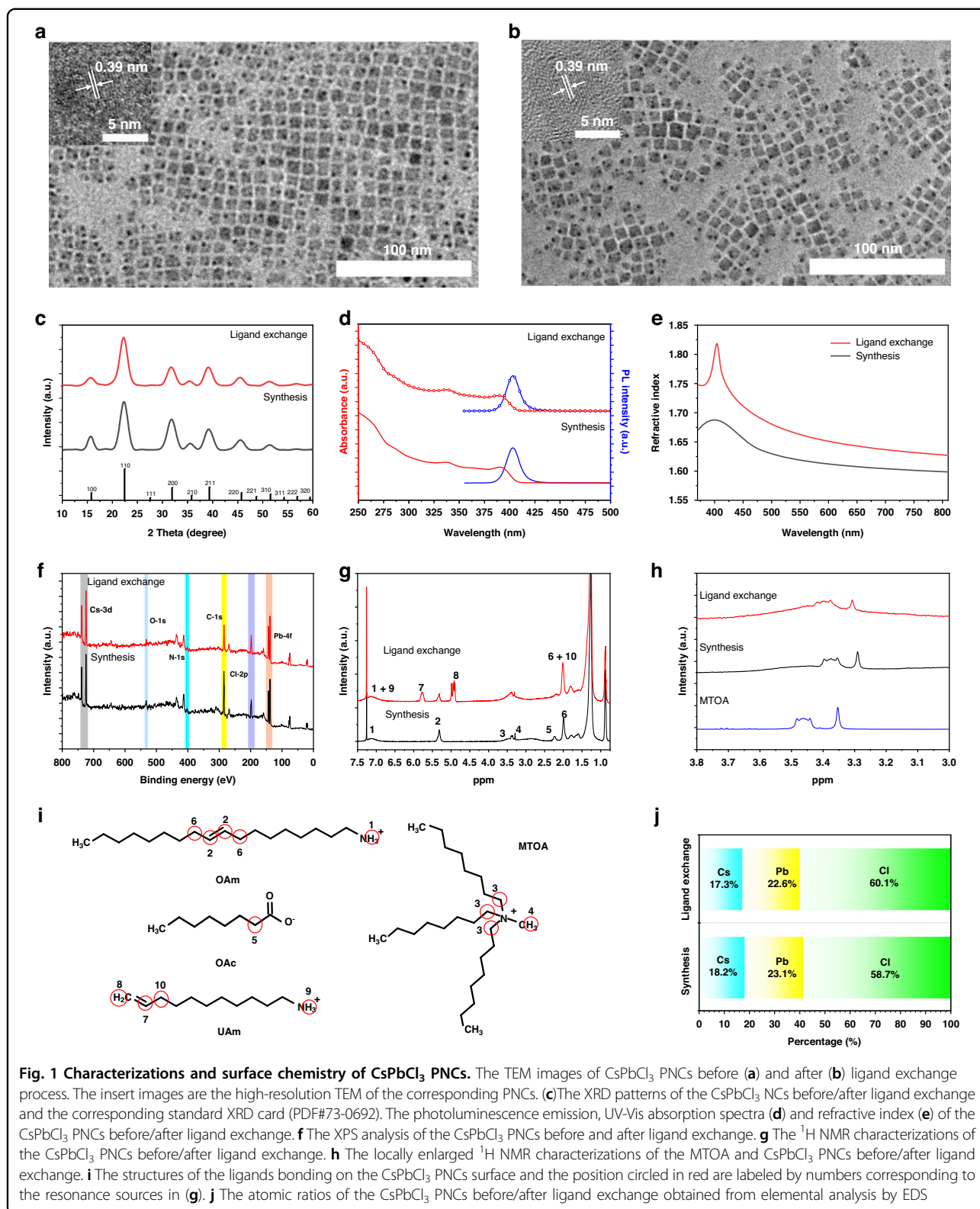
Results

Facile production of styrene-soluble PNCs

The CsPbCl₃ PNCs synthesis was conducted at room temperature. We first utilized methyltrioctylammonium chloride (MTOA) to make PbCl₂ dissolve in p-xylene as a Pb-precursor. The cesium octanoate (CsOAc) was injected into Pb-precursor under stirring, during which CsPbCl₃ PNCs nucleated and grew. After a while, long-chain ligand oleylamine (OAm) was added to ensure the stability and dispersibility of CsPbCl₃ PNCs. Then, the surface of as-synthesized pristine PNCs was modified with EAm through a ligand exchange process, after which the PNCs can well disperse in styrene (St), as shown in Supplementary Fig. S1. The pristine PNCs exhibit an average size of about 6–10 nm with distinct lattice fringe of 0.39 nm corresponding to (110) plane (PDF#73-0692) and the modified PNCs exhibit almost the same size. (Fig. 1a, b) The X-ray diffraction (XRD) pattern further confirms both pristine and modified PNCs possess a cubic crystalline perovskite structure (space group: Pm-3m). (Fig. 1c) From the optical spectra of Fig. 1d, both show excitonic absorption peaks at 390 nm and emission peaks at 403 nm with narrow line width of about 15 nm. The refractive index of modified PNCs is much higher than that of pristine PNCs (Fig. 1e), which is attributed to the reduction of ligand content as evidenced by thermogravimetric analysis (TGA) in Supplementary Fig. S2a, b⁴⁷.

Surface chemistry of CsPbCl₃ PNCs

Investigating the PNC surface chemistry is critical for hybridization with PS. Therefore, ¹H nuclear magnetic resonance (NMR), X-ray photoelectron spectroscopy



(XPS) and Energy dispersive spectrometer (EDS) were conducted to identify the PNC surface. The XPS analysis (Fig. 1f) shows no significant changes in core levels after

the ligand exchange process and the corresponding high-resolution XPS spectra of Cs 3d, Pb 4f, Cl 2p and N 1s are presented in Supplementary Fig. S3a–d. The N 1s and

O 1 s core level signals of XPS in combination with the ^1H NMR characterization (Fig. 1g) demonstrate that all the three ligands (OAm, MTOA, OAc) exist on the surface of pristine PNCs. All the sources of the resonances are marked in Fig. 1i. The reference ^1H NMR spectra of the ligands are shown in Supplementary Fig. S4. Ligands bonding to the surface will feature broadened and shifted resonances⁴. The broad resonance 1 ascribes to the protonated amine group ($-\text{NH}_3^+$) of protonated OAm (Fig. 1g), which can further be demonstrated by the N 1 s core level in Supplementary Fig. S3d. As N 1 s signal around 402 eV is ascribed to $-\text{NH}_3^+$ and there is no signal around 400 eV for amine group ($-\text{NH}_2$)⁴⁸. Compared with the reference ^1H NMR spectrum of OAc, the resonance 5 assigned to OAc has slightly shifted from 2.35 ppm to 2.23 ppm caused by deprotonation. Therefore, OAm is protonated with OAc to form oleylammonium octanoate bonding to the PNCs surface, which is coincident with the conclusion of Kovalenko group⁴. As for MTOA, it is also a bound ligand as the resonances 3 and 4 are obviously broadened with slight shifts and can still be detected on the modified PNCs surface (Fig. 1h). The EAm tightly bonds on the modified PNCs surface after ligand exchange treatment demonstrated by the characteristic resonance 7 and 8. The relative molar amount of the main ligand can be calculated roughly, which is EAm: OAm: MTOA = 1: 0.58: 0.36. (Details shown in Supplementary Note 1) The atomic ratio Cs: Pb: Cl of pristine and modified PNCs is 1: 1.27: 3.23 and 1: 1.30: 3.47 (Fig. 1j). After modification, the ratios of Pb/Cs and Cl/Cs are much higher than the theoretical value, indicating that the PNCs have a Cs-poor surface. We ascribe the formation of the Cs-poor surface to the Cs-poor synthesis condition as Cs: Pb: Cl = 1: 4.5: 18.

The fabrication of PNCs/PS nanocomposites

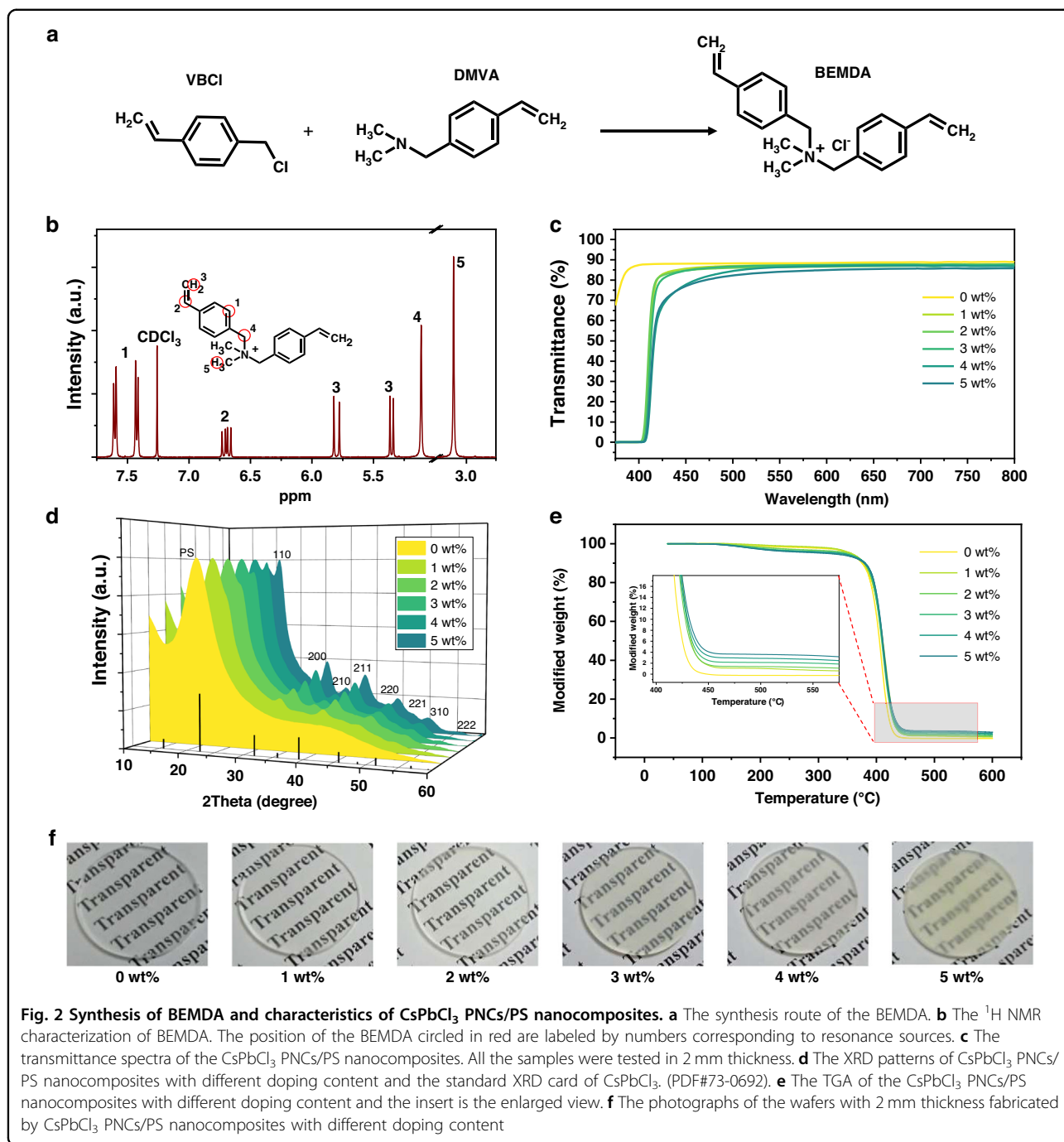
Though EAm can help PNCs disperse in St, the EAm has an extremely low polymerization activity, resulting in the precipitation of the modified PNCs during a subsequent polymerization process. (Supplementary Fig. S5a, b) To enhance the compatibility of PNCs with PS, we synthesized a kind of quaternary ammonium salt (BEMDA) with high polymerization activity as another kind of surfactant shown in Fig. 2a and the corresponding NMR analysis is shown in Fig. 2b. The nanocomposites can still maintain a high level of transmittance when the doping content is up to 3 wt%. (Fig. 2c) The high transmittance can be ascribed to the even distribution of PNCs in PS as shown in TEM after ultra-thin section treatment (Supplementary Fig. S6a–e) and the PNCs still show a small size after hybridization. When the particle size is much less than the light wavelength, the light scattering by the particles can be described by Rayleigh scattering theory^{49–51}, which accounts for the high transmittance of

the nanocomposites. Typically, the size range of the particle is less than one-tenth of the light wavelength^{52,53}. When the doping content increased to 4 wt%, the PNCs begin to show a slight aggregation, therefore the transmittance decreases slightly. From the XRD pattern (Fig. 2d), the diffraction intensity gradually increases as the doping content increases from 0 wt% to 5 wt% and the crystalline structure of PNCs remains unchanged. To identify the doping content, we conducted a thermogravimetric (TGA) analysis (Fig. 2e and Supplementary Table S1), which shows negligible differences between theoretical and actual doping content. The photographs of bulk wafers fabricated by CsPbCl_3 PNCs/PS nanocomposites with different doping content are shown in Fig. 2f.

Surface illuminance performance of LGP based on PNCs/PS nanocomposites

As PS is an important kind of optical waveguide material due to its high refractive index⁵⁴, we found the CsPbCl_3 PNCs with higher refractive index can scatter the light conducting in bulk PS without serious extinction due to the Rayleigh scattering property⁵⁵. As shown in Fig. 3a we could intuitively observe the blue laser light spreads evenly in the bulk plate based on PNCs/PS nanocomposites and the surface luminance is higher than the control. Therefore, the light can keep conducting in the bulk PNCs/PS nanocomposite while enhancing the surface light output without severe loss, indicating a huge potential to serve as LGP in LCD application.

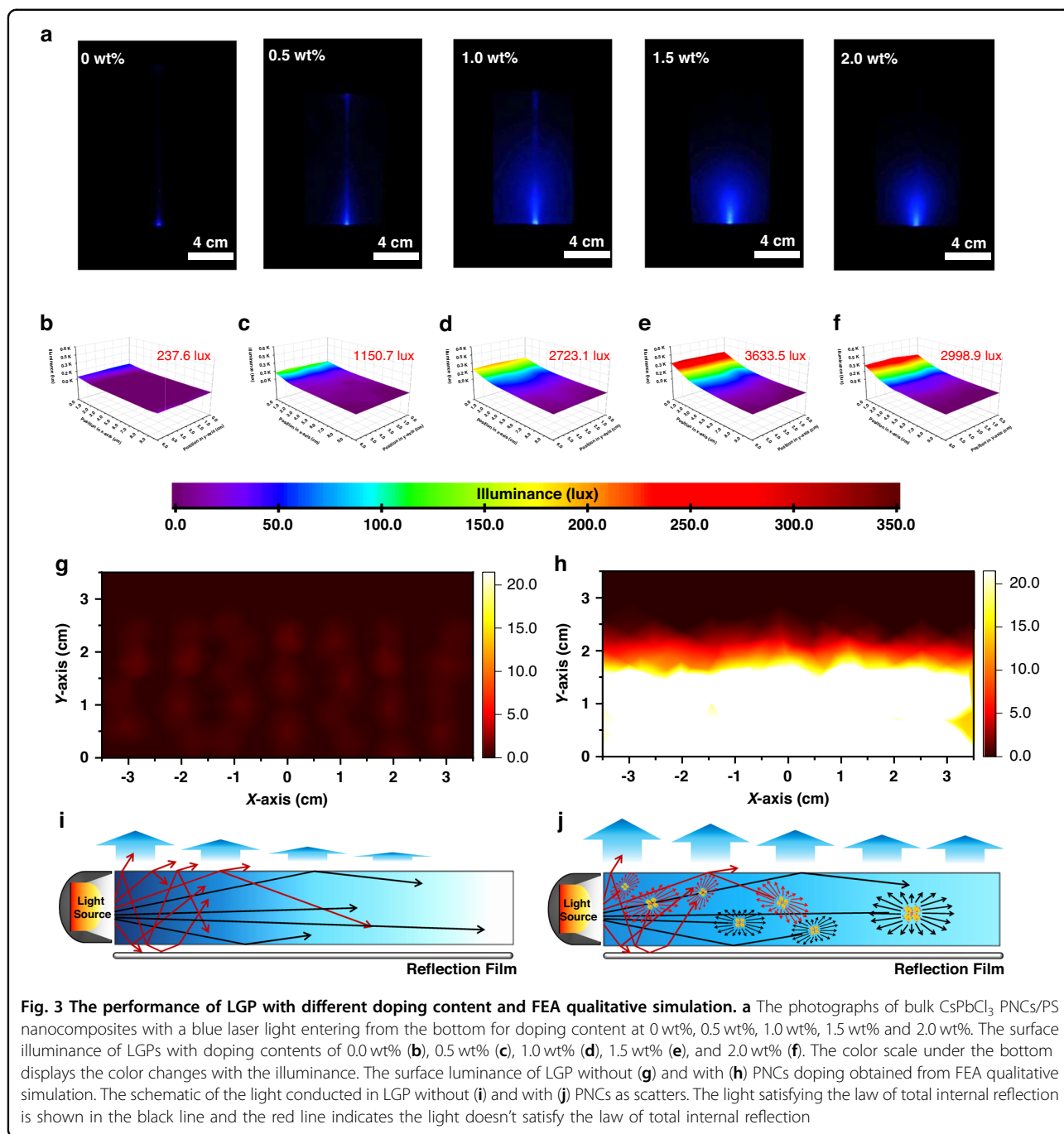
To show the performance of the LGPs, we fabricated large-size bulk nanocomposites up to 5.0 inches with doping contents at 0, 0.5, 1.0, 1.5, and 2.0 wt%. For convenience, the LGP with N wt% doping content is shown in N wt%-LGP. We conducted a surface illuminance test with a blue edge-light source on the short side of the LGP. The test area is at the central large visible area. (Details shown in Supplementary Fig. S7) The illuminance on the surface of the LGP is much higher than that of the control. (Fig. 3b–f) The illuminance of 1.5 wt%-LGP can even reach 3633.5 lux about 15.3 times higher than that of the 0 wt%-LGP. However, when the doping content becomes further higher, the surface illuminance begins to decrease because most of the light is consumed near the light incident edge. The enhancement of the surface illuminance is based on the consumption of the light conducted in the LGP caused by the scattering of the PNCs. When the doping content becomes further higher, the scattering ability of the LGP becomes further higher, correspondingly, most of the light is consumed and output from the light incident edge (as shown in Supplementary Fig. S7 marked as light blue) before it reaches the center display area (marked in dark blue). Therefore, the excellent performance of LGP depends not only on the total illuminance but also on the uniformity,



which means the enhancement of the surface luminance should not be at the severe expense of the conduction distance. Though the 1 wt%-LGP shows a moderate surface illuminance, it shows a slow decay rate as the illuminance can still be detected after 10 cm distance conduction, which means a low illuminance difference in practical display. (Supplementary Fig. S8).

Qualitative simulation based on finite element analysis (FEA) was conducted to show the effect of PNCs on the

light. The light conducting in the LGP can be divided into two parts: the light meets the condition for total internal reflection (L_1) and the light does not (L_2). For the light L_1 , the light will conduct in LGP and will not contribute to the surface illuminance. (Supplementary Fig. S9a) As for the light L_2 , the light will output unevenly from the surface near the light source. (Supplementary Fig. S9b) In this situation, the on-surface output light will exhibit a low luminance and poor



uniformity. (Fig. 3g) However, when there are PNCs inside the LGP, the light L_1 will contribute to the surface luminance (Supplementary Fig. S9c) and the surface luminance from the light L_2 can be uniformized and enhanced (Supplementary Fig. S9d). Therefore, the LGP with PNCs doping shows higher brightness and uniformity than the LGP without PNCs doping. (Fig. 3h) We illustrate the PNCs scattering effect on the light in Fig. 3i, j. The light scattering is according to the Rayleigh scattering.

We extended this strategy to other PNC compositions as the optical properties can be adjusted facily through composition adjustment. The styrene-soluble CsPbCl_xBr_{3-x} ($x = 1.0, 1.5, 2.0, 2.5, 3.0$) PNCs show proper optical characteristics for the conducting light (Supplementary Fig. S10a) and the refractive index gradually increases as the Br component increases. (Supplementary Fig. S10b) The characteristics of the absorption coefficient obtained from spectroscopic ellipsometry are consistent with the absorption spectra demonstrating the veracities of

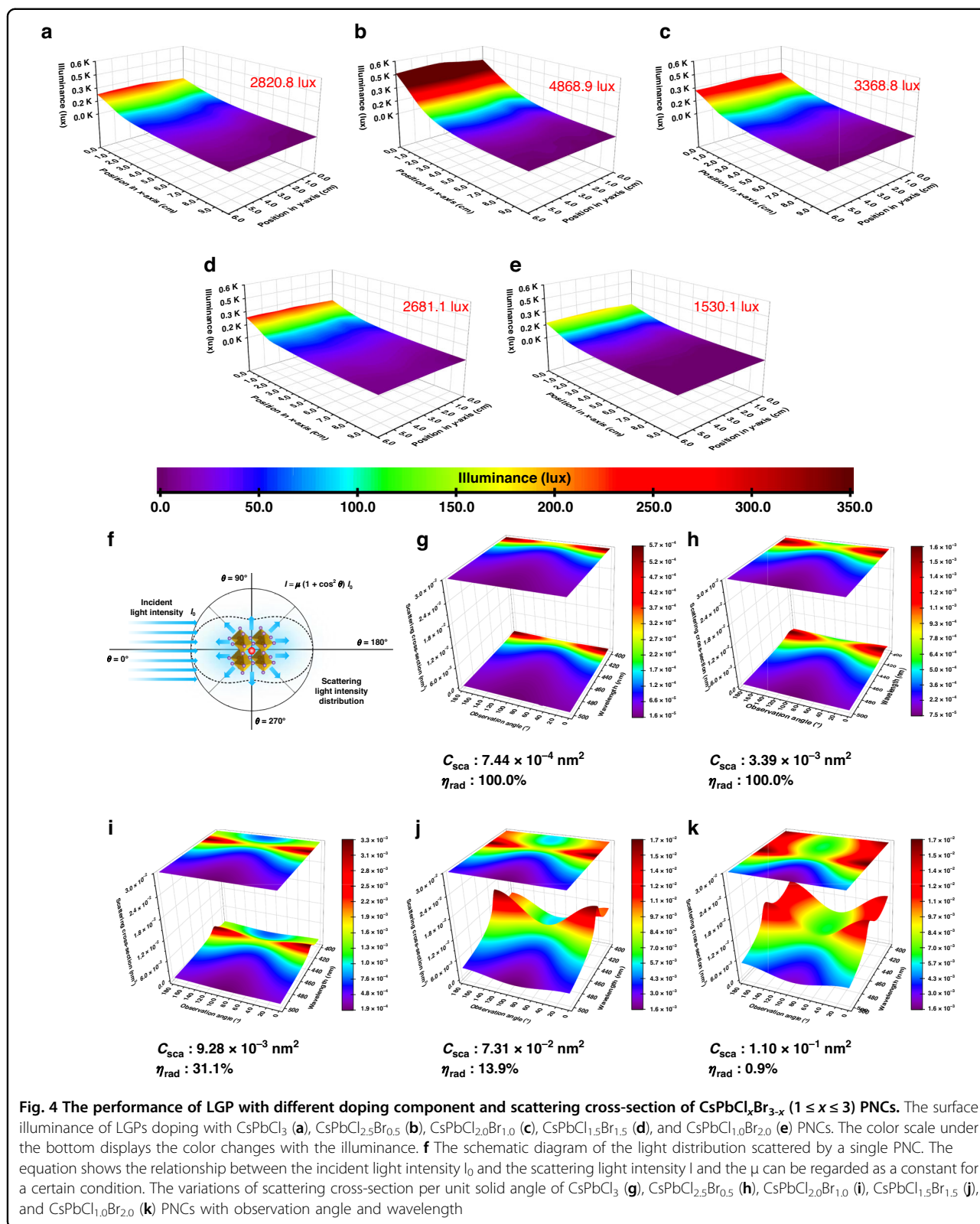
refractive index and absorption coefficient. The refractive indexes are 1.70, 1.74, 1.83, 1.91, 2.02 at 450 nm for CsPbCl_xBr_{3-x} ($x = 1.0, 1.5, 2.0, 2.5, 3.0$) PNCs, respectively. As Br content increases, the CsPbCl_xBr_{3-x} PNCs still maintain a cubic crystalline perovskite structure (space group: Pm-3m) with a slight diffraction peak position shift caused by enlarged interplanar crystal spacing (Supplementary Fig. S10c) and the average crystal size shows a little bit increment from 8 to 11.5 nm. (Supplementary Fig. S11a–f) The XPS spectra of CsPbCl_xBr_{3-x} PNCs are also shown in Supplementary Fig. S12. The nanocomposites doping with 1 wt% CsPbCl_xBr_{3-x} PNCs still show a high transmittance (Supplementary Fig. S13a, b), and the PNCs uniformly disperse in the polymer matrix without aggregation demonstrating the universality of the hybridization method. (Supplementary Fig. S14) We also conducted the surface illuminance test to LGP doping with CsPbCl_xBr_{3-x} PNCs (x -LGP). (Fig. 4a–e) The 2.5-LGP shows the best surface illuminance up to 4868.9 lux about 20.5 times higher than the control LGP in Fig. 3b. The total illuminance will not further improve when the Br content of the PNCs becomes further high due to an obvious absorption of CsPbCl_{1.5}Br_{1.5} and CsPbCl_{1.0}Br_{2.0} PNCs.

The performance of LGP is affected by several factors, mainly including the scatter and absorption of light by PNCs and PNC concentration^{49,51,56}. As for the fluorescence of PNCs, multiple reabsorption processes will result in a negligible influence on the on-surface luminance¹⁶. For a single small PNC, light scattering can be described by Rayleigh scattering theory⁵⁰. Unlike Mie scattering, whose scattering is directional and occurs in narrow angles⁵⁷, the Rayleigh scattering can be regarded as “isotropic scattering” and the light scattered by PNC distributes according to $1 + \cos^2\theta$, where the θ is the observation angle. (Fig. 4f) Therefore, the intensity of the light scattered in the nearly horizontal direction is higher than that in the nearly vertical direction, which means the PNCs can not only make the light homogeneously distribute but also enhance the on-surface luminance. Figure 4g–k illustrates the variations of scattering cross-section per unit solid angle of CsPbCl_xBr_{3-x} PNCs with observation angle and wavelength. All the related calculation details are shown in Supplementary Note 2 and Supplementary Table S2. The scattering cross-section per unit solid angle generally increases and the maximum value for different CsPbCl_xBr_{3-x} PNCs gradually shifts to a longer wavelength as the Br component increases. Therefore, the total scattering cross-section (C_{sca}) is utilized to show the comprehensive scattering effect on the light source, which is defined as the weighted average of the scattering cross-section according to the intensity distribution of the light source. The C_{sca} also gradually increases as the Br component increases, indicating an enhanced scattering ability of PNCs to the light. For

Rayleigh scattering, the C_{sca} of a single PNC is too small to perceive. By taking PNC concentration into account, the volume scattering coefficient (k_{sca}) can be regarded as the ability to scatter the light in LGP per unit volume⁵⁶. The k_{sca} are 3.86×10^{-8} , 1.48×10^{-7} , 2.09×10^{-7} , 1.05×10^{-6} and $6.86 \times 10^{-7} \text{ nm}^{-1}$ for x -LGP ($x = 3.0, 2.5, 2.0, 1.5, 1.0$), respectively. Whereas, the absorption of the PNCs cannot be ignored, especially for CsPbCl_xBr_{3-x} ($1.0 \leq x \leq 2.0$) PNCs. Optical radiation efficiency (η_{rad}) represents the fraction of scattering light out of the extinction, which shows a comparison of the scattering and the absorption effect on the light^{56,58}. The η_{rad} of CsPbCl₃ and CsPbCl_{2.5}Br_{0.5} PNCs are both 100.0%, which means the illuminance is only affected by k_{sca} . Therefore, 2.5-LGP shows a higher illuminance than 3-LGP. The η_{rad} of CsPbCl_{2.0}Br_{1.0} PNCs begins to decrease, leading to a reduction of illuminance for 2-LGP. But when compared with 3-LGP, the comprehensive influence of CsPbCl_{2.0}Br_{1.0} PNCs is still positive to the illuminance due to the higher k_{sca} . The illuminance of 1.5-LGP drops to 2681.1 lux even lower than 3-LGP caused by the significant reduction of η_{rad} . When the ratio of Br: Cl becomes further higher, the η_{rad} becomes extremely low up to 0.73% and most of the light is absorbed by CsPbCl_{1.0}Br_{2.0} PNCs, leading to a serious loss of illuminance. The spectra of the light output from different LGPs are shown in Supplementary Fig. S15. The spectrum of the output light began to show an obvious change from LGP doping with CsPbCl_{1.5}Br_{1.5} PNCs as there is a notable absence of light <430 nm. When the ratio of Br becomes further high, the optical peak even changes from 450 to 463 nm. The changes of the optical spectra are mainly attributed to the absorption of the PNCs inside the LGP.

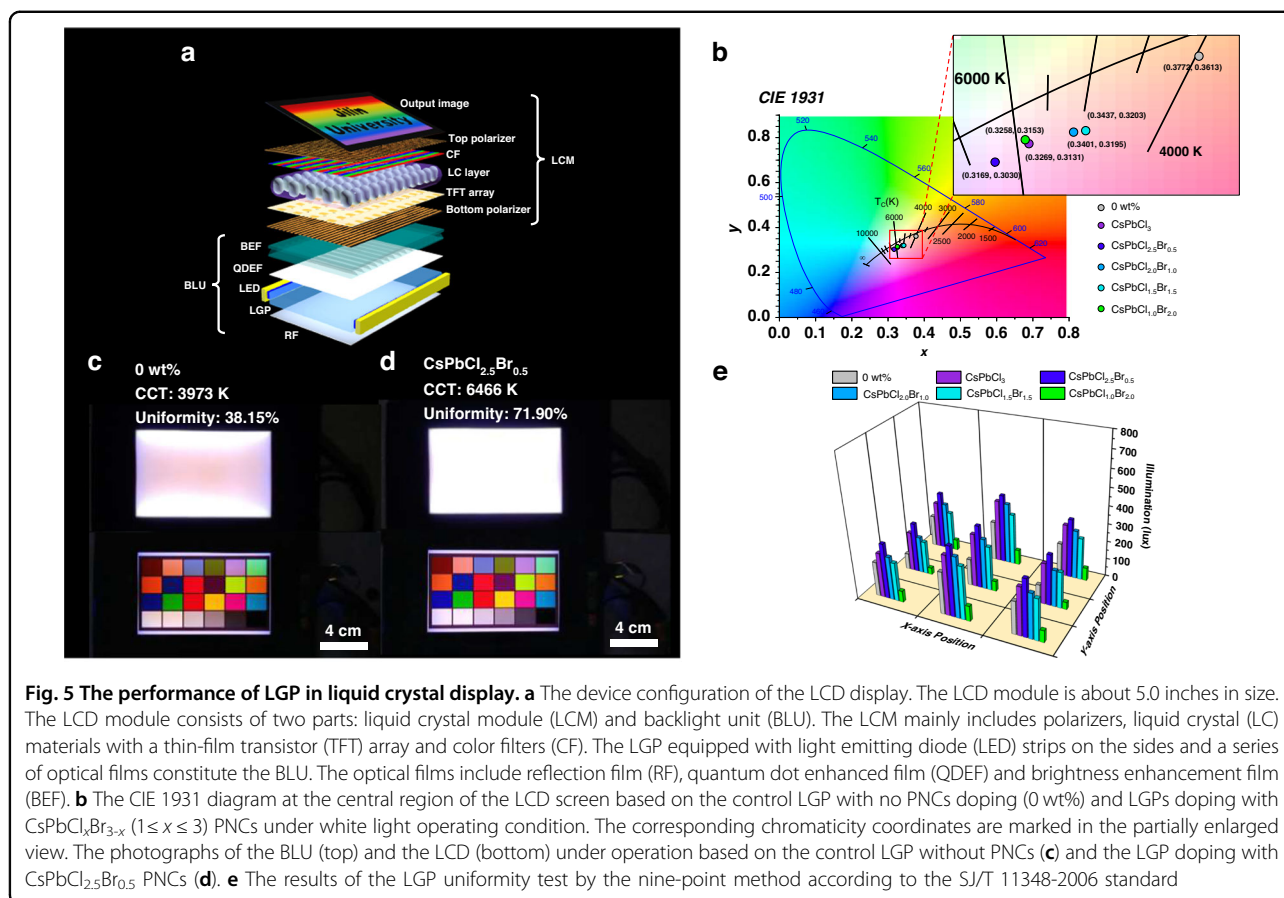
Performance in liquid crystal display

We explored the commercial potential by integrating the LGP with advanced display technology^{59,60}. The device configuration is typical (Fig. 5a), where the blue edge-light source is converted into surface light by LGP and passes through the quantum dot enhanced film (QDEF) and brightness enhancement film (BEF) for color conversion and brightness enhancement. Finally, the liquid crystal module (LCM) controls the illuminating light to show various images. The CIE 1931 diagram (Fig. 5b) shows all the chromaticity coordinates of the LCDs under white light operating mode. The correlated color temperature (CCT) of the LCD generally increases with the surface illuminance of LGP as the blue light component increases (Supplementary Fig. S16). While the CCT based on 1.0-LGP is abnormally higher than that based on 3.0-LGP, we ascribe it to the obviously changed optical distribution of output light (Supplementary Fig. S15). The peak of the output light is changed from 450 nm to 465 nm and there is almost no light distribution <440 nm due to the absorption of the



$\text{CsPbCl}_{1.0}\text{Br}_{2.0}$ PNCs. The changed optical distribution will influence the light conversion of QDEF. Therefore, we further characterized the absorption and fluorescence

spectrum of the QDEF (Supplementary Fig. S17). The result of the uniformity test according to SJ/T 11348-2006 standard is shown in Fig. 5e and details are



presented in Supplementary Fig. S18 and Supplementary Table S3. The uniformities under lab level are 38.15%, 63.32%, 71.90%, 59.10%, 62.78%, and 45.55% for the control, 3.0, 2.5, 2.0, 1.5, and 1.0-LGP, respectively. All the uniformities based on LGP show obvious improvement. Figure 5c, d show the backlight unit (BLU) and LCD quality based on the control and the best-performing 2.5-LGP. For other LGPs, the photographs of display quality are shown in Supplementary Fig. S19. The control BLU exhibits an obvious difference between the central region and the edge region. However, the performance of BLU based on 2.5-LGP shows a huge promotion both in illuminance and uniformity. The improvement in luminance also means a reduction in electric power consumption as LGP equipped with a low-intensity light source can achieve a better surface luminance than a normal LGP equipped with a very high-consumption light source does. To test the stability of the LGP, we first measured the fluorescence spectra of the nanocomposites with 1 wt% as shown in Supplementary Fig. S20a. Based on the characterization, we further observed the photoluminescence (PL) intensity changes of nanocomposite doping with $\text{CsPbCl}_{1.0}\text{Br}_{2.0}$ PNCs under 50 W UV-irradiation and in water to show

the UV and humidity stability, respectively. As shown in Supplementary Fig. S20b, c, the PL intensity only dropped by roughly 20% under continuous irradiation with UV light for about 100 h and there is almost no change of the PL intensity for the sample immersing in water, indicating a high humidity resistance. The excellent performance of LGP in display quality and energy consumption shows a huge potential in practical application.

Discussion

In summary, we successfully fabricated bulk $\text{CsPbCl}_x\text{Br}_{3-x}$ PNCs/PS nanocomposites by a two-type ligand strategy, where the PNCs disperse uniformly in the polymer matrix without aggregation. Further, the Rayleigh scattering behavior of the nanocomposites can be adjusted by the PNC composition adjustment. Based on this property, we first used PNCs as a kind of scatters inside LGP, which could improve the illuminance and uniformity at the same time. We believe this kind of LGP has huge potential in LCD applications and will draw much attention in LGP-related fields, especially as a base material to combine with the advanced LGP processing technologies such as the micro-optical pattern on the bottom or the adoption of the wedge-shaped plates.

Materials and methods

Chemicals

Lead chloride (PbCl_2 , 99.999%), lead bromide (PbBr_2 , 99.999%) and cesium carbonate (Cs_2CO_3 , 99.995%) were purchased from Sigma-Aldrich. Oleylamine (OAm, 90%), undec-10-en-1-amine (EAm, 95%), octanoic acid (OAc, 99%), anhydrous *p*-xylene (99%), methyltrioctylammonium chloride (MTOA, 97%), methyltrioctylammonium bromide (MTOABr, 98%), 4-vinylbenzyl chloride (VBCl, 98%), methyl acetate (MeOAc, 99%), 2,2'-Azobis(2,4-dimethyl)valeronitrile (ABVN, 98%) and styrene (St, 99%) were purchased from Macklin reagent. *N,N*-dimethyl-4-vinylaniline (DMVA, 90%) was purchased from Acros Organics.

Synthesis of $\text{CsPbCl}_x\text{Br}_{3-x}$ PNCs

The preparation and purification of CsPbCl_3 PNCs were conducted at room temperature in open air. First, Cs_2CO_3 (1 mmol) was dissolved in OAc (10 mL) to obtain cesium octanoate (CsOAc) solution. Second, 0.9 mmol of PbCl_2 and 1.8 mmol of MTOA were dissolved into 9 mL anhydrous *p*-xylene to obtain Pb-precursor solution. Then, CsOAc solution (1 mL) was swiftly injected into the as-prepared Pb-precursor under vigorous stirring. After about 30 s, OAm (1 mL) was added and stirred for 2 min. Subsequently, MeOAc was added into the crude solution with a volume ratio of 3:1. The precipitation was collected by centrifugation at 9000 rpm and re-dispersed in 3 mL hexane for ligand exchange treatment. For the synthesis of $\text{CsPbCl}_x\text{Br}_{3-x}$, all the processes were the same under the corresponding ratios of PbCl_2 to PbBr_2 and MTOA to MTOABr.

Modification of PNCs

For ligand exchange treatment, EAm (50 μL) was added to the above PNCs dissolved with 3 mL hexane solution. After stirring for 5 min, MeOAc (12 mL) was added to precipitate the modified PNCs and centrifuged at 9000 rpm. The obtained PNCs powder was completely dry under vacuum for further use.

Synthesis of BEMDA

The synthesis of quaternary ammonium salt is based on the previous study with some changes⁶¹. Briefly, 3.584 g of DMVA and 3.114 g of VBCl were mixed in acetone (60 mL). The mixture was stirred and refluxed at 45 °C overnight. The precipitated BEMDA in the mixture was purified and recrystallized by acetone/ether. The product was further washed to white by ether. ¹H-NMR (CDCl_3 , 400 MHz): 7.26–7.61 (m, 8H, ArH), 6.66–6.73 (m, 2H, ArCH=), 5.34–5.82 (m, 4H, ArCH=CH₂), 5.11 (s, 4H, ArCH₂-N⁺), 3.11 (s, 6H, N⁺-CH₃).

Fabrication of PNCs/PS nanocomposites

The stabilizer was removed from St monomer before use. The modified PNCs with corresponding weight, BEMDA, 1 wt% ABVN were mixed in St solution. The weight of BEMDA was about one-tenth of the modified PNCs' weight. The mixture was stirred until clear and pre-polymerized for 16 h under 50 °C. Subsequently, the viscous oligomer was injected into the mold and degassed until there are no bubbles in the system. After the injection, the mold was further heated at 60 °C for 36 h to make the polymerization complete.

Characterizations

UV-visible absorption spectra were obtained using a Shimadzu 3600 UV-visible-NIR spectrophotometer and photoluminescence (PL) spectra on a Cary Eclipse spectrofluorimeter. Nuclear magnetic resonance spectra (NMR) were collected from a Zhongke-Niujin Nuclear magnetic resonance spectrometer 400 MHz in deuterated chloroform. The refractive index and absorption efficient were measured via a variable angle spectroscopic ellipsometer (J.A. Woollam Co., Inc., USA) with the UV-vis-NIR range from 1.24 to 4.13 eV. The ellipsometric angle ψ and phase difference Δ were recorded at incidence angles of 55, 65, and 75°, respectively. The detail morphology of the samples was observed on a JEM-2100F at an accelerating voltage of 200 kV via a transmission electron microscopy (TEM). Energy Disperse Spectroscopy (EDS) for elemental analysis was conducted on a Bruker Energy Dispersive Spectrometer based on a SU8020 electron microscope. X-ray diffraction (XRD) data were collected using a PANalytical B.V.-Empyrean Diffractometer with Cu K α radiation. X-ray photoelectron spectroscopy (XPS) were measured in an integrated ultrahigh vacuum system equipped with multitechnique surface analysis system (VG ESCALAB MK II spectrometer). The transmittance test of material was conducted on an UV-visible-NIR spectrophotometer from PerkinElmer company. Thermogravimetric analysis (TGA) was conducted on NETZSCH STA449F3 QMS403D/Bruker V70 in N₂ atmosphere with 10 °C min⁻¹ heating rate. The ultrathin section treatment to the nanocomposites was conducted by a Leica EM UC7 cryo-cut microtome. The illuminance test was conducted by an illuminometer from Suzhou TASI Electronics. The chromaticity coordinate, correlated color temperature and corresponding optical spectrum were tested by a photometer SPIC-300BW from EVERFINE.

Qualitative simulation based on finite element analysis (FEA)

The FEA simulation was conducted based on practical condition, such as the material of LGP and the refractive index of PNCs at 450 nm. The boundary conditions of LGP were set as specular reflection on the bottom and

elimination on sides. The light scattering distribution was manually controlled as Rayleigh distribution. The surface brightness was obtained by frozen wall with accumulation condition.

Acknowledgements

This work was financially supported by the National Science Foundation of China (NSFC) under Grant No. 52233005.

Author contributions

C.L. proposed the original research idea and contributes mainly to the work under the guidance of B.Y. K.Z. provided necessary advices on experiment, data analysis and paper revision. Z.Z., K.P., and Y.F. assisted with characterizations including transmission electron microscope characterization, X-ray photoelectron spectroscopy, and energy disperse spectroscopy.

Data availability

The data that support the plots within this paper and the other findings of this study are available from the corresponding authors upon reasonable request.

Conflict of interest

The authors declare no competing interests.

Supplementary information The online version contains supplementary material available at <https://doi.org/10.1038/s41377-023-01306-z>.

Received: 27 July 2023 Revised: 9 October 2023 Accepted: 12 October 2023
Published online: 01 November 2023

References

- Liu, C. M. et al. Metal halide perovskite nanocrystal solar cells: progress and challenges. *Small Methods* **4**, 2000419 (2020).
- Akkerman, Q. A. et al. Genesis, challenges and opportunities for colloidal lead halide perovskite nanocrystals. *Nat. Mater.* **17**, 394–405 (2018).
- Kovalenko, M. V., Protesescu, L. & Bodnarchuk, M. I. Properties and potential optoelectronic applications of lead halide perovskite nanocrystals. *Science* **358**, 745–750 (2017).
- De Roo, J. et al. Highly dynamic ligand binding and light absorption coefficient of cesium lead bromide perovskite nanocrystals. *ACS Nano* **10**, 2071–2081 (2016).
- Liang, S. et al. Recent advances in synthesis, properties, and applications of metal halide perovskite nanocrystals/polymer nanocomposites. *Adv. Mater.* **33**, 2005888 (2021).
- Jin, G. et al. Aqueous-processed polymer/nanocrystal hybrid solar cells with double-side bulk heterojunction. *Adv. Energy Mater.* **8**, 1701966 (2018).
- Strein, E. et al. Charge generation and energy transfer in hybrid polymer/infrared quantum dot solar cells. *Energy Environ. Sci.* **6**, 769–775 (2013).
- Li, L. M. et al. Assembling a lasing hybrid material with supramolecular polymers and nanocrystals. *Nat. Mater.* **2**, 689–694 (2003).
- Han, M. Y. et al. Quantum-dot-tagged microbeads for multiplexed optical coding of biomolecules. *Nat. Biotechnol.* **19**, 631–635 (2001).
- Cohen, T. A. et al. Modular zwitterion-functionalized poly (isopropyl methacrylate) polymers for hosting luminescent lead halide perovskite nanocrystals. *Chem. Mater.* **33**, 3779–3790 (2021).
- Ji, K. et al. High-efficiency perovskite quantum dot solar cells benefiting from a conjugated polymer-quantum dot bulk heterojunction connecting layer. *J. Mater. Chem. A* **8**, 8104–8112 (2020).
- Yang, Y. et al. Flexible polymer-assisted mesoscale self-assembly of colloidal CsPbBr₃ perovskite nanocrystals into higher order superstructures with strong inter-nanocrystal electronic coupling. *J. Am. Chem. Soc.* **141**, 1526–1536 (2019).
- Yoon, Y. J. et al. Enabling tailorable optical properties and markedly enhanced stability of perovskite quantum dots by permanently ligating with polymer hairs. *Adv. Mater.* **31**, 1901602 (2019).
- He, Y. J. et al. Unconventional route to dual-shelled organolead halide perovskite nanocrystals with controlled dimensions, surface chemistry, and stabilities. *Sci. Adv.* **5**, eaax4424 (2019).
- Ko, J. et al. Ligand-assisted direct photolithography of perovskite nanocrystals encapsulated with multifunctional polymer ligands for stable, full-colored, high-resolution displays. *Nano Lett.* **21**, 2288–2295 (2021).
- Lin, J. D. et al. Perovskite quantum dots glasses based backlit displays. *ACS Energy Lett.* **6**, 519–528 (2021).
- Shi, L. F. et al. In situ inkjet printing strategy for fabricating perovskite quantum dot patterns. *Adv. Funct. Mater.* **29**, 1903648 (2019).
- Zhao, H. G. et al. Zero-dimensional perovskite nanocrystals for efficient luminescent solar concentrators. *Adv. Funct. Mater.* **29**, 1902262 (2019).
- Wu, J. J. et al. Efficient and stable thin-film luminescent solar concentrators enabled by near-infrared emission perovskite nanocrystals. *Angew. Chem. Int. Ed.* **59**, 7738–7742 (2020).
- Heo, J. H. et al. High-performance next-generation perovskite nanocrystal scintillator for nondestructive X-ray imaging. *Adv. Mater.* **30**, 1801743 (2018).
- Gandini, M. et al. Efficient, fast and reabsorption-free perovskite nanocrystal-based sensitized plastic scintillators. *Nat. Nanotechnol.* **15**, 462–468 (2020).
- Yin, W. X. et al. Multidentate ligand polyethylenimine enables bright color-saturated blue light-emitting diodes based on CsPbBr₃ nanoplatelets. *ACS Energy Lett.* **6**, 477–484 (2021).
- Cai, W. Q. et al. Polymer-assisted in situ growth of all-inorganic perovskite nanocrystal film for efficient and stable pure-red light-emitting devices. *ACS Appl. Mater. Interfaces* **10**, 42564–42572 (2018).
- Zhou, Q. C. et al. In situ fabrication of halide perovskite nanocrystal-embedded polymer composite films with enhanced photoluminescence for display backlights. *Adv. Mater.* **28**, 9163–9168 (2016).
- Guijarro, N. et al. Lead halide perovskite quantum dots to enhance the power conversion efficiency of organic solar cells. *Angew. Chem.* **131**, 12826–12834 (2019).
- Wang, Y. F. et al. High-efficiency perovskite quantum dot hybrid non-fullerene organic solar cells with near-zero driving force. *Adv. Mater.* **32**, 2002066 (2020).
- Kim, H. et al. Polymer zwitterions for stabilization of CsPbBr₃ perovskite nanoparticles and nanocomposite films. *Angew. Chem.* **132**, 10894–10898 (2020).
- Li, D. et al. Zinc-methacrylate passivation enables an efficient and stable perovskite nanocrystal-polymer composite for LED applications. *J. Mater. Chem. C* **9**, 2873–2881 (2021).
- Chaudhary, D. K. et al. Charge transport between coaxial polymer nanorods and grafted all-inorganic perovskite nanocrystals for hybrid organic solar cells with enhanced photoconversion efficiency. *J. Phys. Chem. C* **124**, 246–255 (2020).
- Pan, A. Z. et al. General strategy for the preparation of stable luminous nanocomposite inks using chemically addressable CsPbX₃ perovskite nanocrystals. *Chem. Mater.* **30**, 2771–2780 (2018).
- Kim, H. et al. Functional polymers for growth and stabilization of CsPbBr₃ perovskite nanoparticles. *Chem. Commun.* **55**, 1833–1836 (2019).
- Chang, S., Bai, Z. L. & Zhong, H. Z. In situ fabricated perovskite nanocrystals: a revolution in optical materials. *Adv. Opt. Mater.* **6**, 1800380 (2018).
- Cai, Y. T. et al. Improved stability of CsPbBr₃ perovskite quantum dots achieved by suppressing interligand proton transfer and applying a polystyrene coating. *Nanoscale* **10**, 21441–21450 (2018).
- Pan, A. Z. et al. Nanorod suprastructures from a ternary graphene oxide-polymer-CsPbX₃ perovskite nanocrystal composite that display high environmental stability. *Nano Lett.* **17**, 6759–6765 (2017).
- Zhang, H. H. et al. Embedding perovskite nanocrystals into a polymer matrix for tunable luminescence probes in cell imaging. *Adv. Funct. Mater.* **27**, 1604382 (2017).
- Wu, H. et al. Ultrastable inorganic perovskite nanocrystals coated with a thick long-chain polymer for efficient white light-emitting diodes. *Chem. Mater.* **31**, 1936–1940 (2019).
- Jiang, G. C. et al. Highly luminescent and water-resistant CsPbBr₃-CsPb₂Br₅ perovskite nanocrystals coordinated with partially hydrolyzed poly (methyl methacrylate) and polyethylenimine. *ACS Nano* **13**, 10386–10396 (2019).
- Sun, H. Z. et al. Chemically addressable perovskite nanocrystals for light-emitting applications. *Adv. Mater.* **29**, 1701153 (2017).

39. Cai, Y. T. et al. A facile synthesis of water-resistant CsPbBr₃ perovskite quantum dots loaded poly (methyl methacrylate) composite microspheres based on in situ polymerization. *Adv. Opt. Mater.* **7**, 1901075 (2019).
40. Liu, Y. C. et al. Tough, stable and self-healing luminescent perovskite-polymer matrix applicable to all harsh aquatic environments. *Nat. Commun.* **13**, 1338 (2022).
41. He, C. J. et al. Refractive index dispersion of organic-inorganic hybrid halide perovskite CH₃NH₃PbX₃ (X=Cl, Br, I) single crystals. *Cryst. Res. Technol.* **54**, 1900011 (2019).
42. Lamichhane, A. & Ravindra, N. M. Energy gap-refractive index relations in perovskites. *Materials* **13**, 1917 (2020).
43. Brittman, S. & Garnett, E. C. Measuring *n* and *k* at the microscale in single crystals of CH₃NH₃PbBr₃ perovskite. *J. Phys. Chem. C* **120**, 616–620 (2016).
44. Ziang, X. et al. Refractive index and extinction coefficient of CH₃NH₃PbI₃ studied by spectroscopic ellipsometry. *Opt. Mater. Express* **5**, 29–43 (2015).
45. He, S. W. et al. Tailoring the refractive index and surface defects of CsPbBr₃ quantum dots via alkyl cation-engineering for efficient perovskite light-emitting diodes. *Chem. Eng. J.* **425**, 130678 (2021).
46. Werner, J. et al. Complex refractive indices of cesium-formamidinium-based mixed-halide perovskites with optical band gaps from 1.5 to 1.8 eV. *ACS Energy Lett.* **3**, 742–747 (2018).
47. Lü, C. et al. A facile Route to ZnS-polymer nanocomposite optical materials with high nanophase content via γ -ray irradiation initiated bulk polymerization. *Adv. Mater.* **18**, 1188–1192 (2006).
48. Zhang, C. Y. et al. Narrow-band violet-light-emitting diodes based on stable cesium lead chloride perovskite nanocrystals. *ACS Energy Lett.* **6**, 3545–3554 (2021).
49. van de Hulst, H. C. *Light Scattering by Small Particles* (Dover Publications, 1981).
50. Horvath, H. Gustav Mie and the scattering and absorption of light by particles: historic developments and basics. *J. Quant. Spectrosc. Radiat. Transf.* **110**, 787–799 (2009).
51. Bohren, C. F. et al. *Absorption and Scattering of Light by Small Particles* (Wiley, 1998).
52. Lü, C. L. & Yang, B. High refractive index organic-inorganic nanocomposites: design, synthesis and application. *J. Mater. Chem.* **19**, 2884–2901 (2009).
53. Batchelder, J. S. & Taubenblatt, M. A. Interferometric detection of forward scattered light from small particles. *Appl. Phys. Lett.* **55**, 215–217 (1989).
54. Ma, H., Jen, A. K. Y. & Dalton, L. R. Polymer-based optical waveguides: materials, processing, and devices. *Adv. Mater.* **14**, 1339–1365 (2002).
55. Novak, B. M. Hybrid nanocomposite materials—between inorganic glasses and organic polymers. *Adv. Mater.* **5**, 422–433 (1993).
56. McCartney, E. J. *Optics of the Atmosphere: Scattering by Molecules and Particles* (Wiley, 1976).
57. Kivshar, Y. Mie scattering yields chiral nonlinearity. *Nat. Photonics* **16**, 89–90 (2022).
58. Tanabe, K. Optical radiation efficiencies of metal nanoparticles for optoelectronic applications. *Mater. Lett.* **61**, 4573–4575 (2007).
59. Luo, Z. Y., Xu, D. M. & Wu, S. T. Emerging quantum-dots-enhanced LCDs. *J. Disp. Technol.* **10**, 526–539 (2014).
60. Chen, H. W., He, J. & Wu, S. T. Recent advances on quantum-dot-enhanced liquid-crystal displays. *IEEE J. Sel. Top. Quantum Electron.* **23**, 1–11 (2017).
61. Aoyagi, T. et al. Polymerization of benzalkonium chloride-type monomer and application to percutaneous drug absorption enhancer. *J. Control. Release* **13**, 63–71 (1990).